Article

Effects of Varying Volume Fractions of SiO$_2$ and Al$_2$O$_3$ on the Performance of Concentrated Photovoltaic System

Muhammad Asim [1], Muhammad Hanzla Tahir [2], Ammara Kanwal [1], Fahid Riaz [3,*], Muhammad Amjad [4,5], Aamna Khalid [1], Muhammad Mujtaba Abbas [4,*], Ashfaq Ahmad [1] and Mohammad Abul Kalam [6]

[1] Department of Mechanical Engineering, University of Engineering & Technology, Lahore 54890, Pakistan; masim381@uet.edu.pk (M.A.)

[2] Department of Energy System Engineering, Pir Mehr Ali Shah Arid Agriculture University, Rawalpindi 46300, Pakistan; muhammadhanzlatahir@uaar.edu.pk

[3] Mechanical Engineering Department, Abu Dhabi University, Abu Dhabi P.O. Box 59911, United Arab Emirates

[4] Department of Mechanical Engineering, University of Engineering and Technology, Lahore (New Campus), Lahore 54890, Pakistan

[5] Chair of Thermodynamics, School of Engineering and Design, Technical University of Munich, 85748 Garching, Germany

[6] School of Civil and Environmental Engineering, FEIT, University of Technology Sydney, Sydney, NSW 2007, Australia

* Correspondence: fahid.riaz@adu.ac.ae (F.R.); m.mujtaba@uet.edu.pk (M.M.A.)

Abstract: Highly concentrated triple-junction solar cells (HCTJSCs) are cells that have diverse applications for power generation. Their electrical efficiency is almost 45%, which may be increased to 50% by the end of the year 2030. Despite their overwhelming ability to generate power, their efficiency is lower when utilized in a concentrated manner, which introduces a high-temperature surge, leading to a sudden drop in output power. In this study, the efficiency of a 10 mm × 10 mm multijunction solar cell (MJSC) was increased to almost 42% under the climatic conditions in Lahore, Pakistan. Active cooling was selected, where SiO$_2$–water- and Al$_2$O$_3$–water-based nanofluids with varying volume fractions, ranging from 5% to 15% by volume, were used with a 0.001 kg/s mass flow rate. In addition, two- and three-layer microchannel heat sinks (MCHSs) with squared microchannels were designed to perform thermal management. Regarding the concentration ratio, 1500 suns were considered for 15 August at noon, with 805 W/m^2 and 110 W/m^2 direct and indirect radiation, respectively. A complete model including a triple-junction solar cell and allied assemblies was modeled in Solidworks software, followed by temperature profile generation in steady-state thermal analyses (SSTA). Thereafter, a coupling of SSTA and Ansys Fluent was made, in combination with the thermal management of the entire model, where the temperature of the TJSC was found to be 991 °C without active cooling, resulting in a decrease in electrical output. At 0.001 kg/s, the optimum average surface temperature (44.5 °C), electrical efficiency (41.97%), and temperature uniformity (16.47 °C) were achieved in the of MJSC with SiO$_2$–water nanofluid with three layers of MCHS at a 15% volume fraction. Furthermore, the average outlet temperature of the Al$_2$O$_3$–water nanofluid at all volume fractions was high, between 29.53 °C and 31.83 °C, using the two-layer configuration. For the three-layer arrangement, the input and output temperatures of the working fluid were found to be the same at 25 °C.

Keywords: highly concentrated triple-junction solar cell; steady-state thermal analysis; computational fluid dynamic analysis; nanofluids; electrical efficiency

1. Introduction

As the price of energy increases around the world, consumers are looking for new ways to obtain energy to meet the growing demand. The amount of energy from the sun that reaches the Earth's surface every four hours is more than what all humans use in a

year. So, obtaining energy from the sun is a great way to achieve this task [1]. As such, solar thermal and photovoltaic (PV) technologies are now used globally to meet the energy demand. Moreover, using PV technology, electricity can be directly create from sunlight; by using solar thermal technology, the heat from the sun can be converted into thermal energy that can be used later in industrial applications [2]. Furthermore, enhancing PV thermoelectric potential is one way to improve the overall performance of an entire system. In this way, the heat that would have been wasted is used as an extra source of energy [3].

Hybrid photovoltaic/thermal (PV/T) systems are coupled with a heat exchanger under the PV cell layer to collect undesired heat. The prime object of PV/T technology is to generate heat at a low operating temperature condition of around 90 °C. However, when the temperature rises, the efficiency of PV cells decreases; hence, it is crucial to maintain a PV cell's surface by using artificial means [4,5]. On the other hand, by expanding the typical PV system of power plant to cope with a short fall in energy demand and supply, the cost of the entire PV system is high and the payback period is long. In addition, any decrease in efficiency has a drastic impact on the life cycle and payback period of a power plant facility. Regarding highly concentrated photovoltaic (HCPV) systems, the price of electricity from PV systems would likely decrease if these III-V multi-junction (MJ) solar cells are used and integrated with concentrators to increase the solar intensity. The main advantages of HCPV systems are their low cost and high efficiency, which lets them produce more electrical power using a smaller area than conventional PV cells [1,6].

When operating HCPV systems, keeping the solar cells cool is one of the most important aspects [7]. When triple-junction solar cells receive large amounts of solar intensity, they heat up, and as the temperature increases, the efficiency and power output of the cells lower. It is important to use a cooling method that works in a way to improve the efficiency of the CPV systems [8]. Case studies were examined in two extensive studies, both of which encompassed several cooling approaches for CPV and PV installations, including the direct liquid-immersion cooling (LIC) methodology. In the CPV systems, only heat pipes, impinging jets, and microchannels achieved low thermal resistance [9]. In another study under 500 suns and a 25 °C atmosphere temperature, the electrical properties of GaInP/GaInAs-/Ge triple-junction solar cells immersed in dimethyl silicon oil with thicknesses of 1.0–30.0 mm were studied using the liquid-immersion cooling (LIC) method in a high-concentrating photovoltaic (CPV) system to control the temperature of the solar cells. The theoretical photocurrent losses of three sets of sub cells caused by the spectral absorption of silicon oil were estimated, and the electrical performance changes of a cell running in silicon oil were closely studied [10].

To compare the temperatures of MJSCs, different methods of cooling are available in the literature at different low CR values, showing that the temperature of the solar cell drops the most when microchannels are used. It was also found that the temperature profile of the cell is better when standard wide microchannel heat sinks are used. In this setup, the only way to lower the temperature difference between the cells is to speed up the flow of the coolant [11]. Additionally, when the flow rate increases, the pump needs more power. Because of this, authors [12] examined how five different microchannel heat sinks could be used to make the temperature of the cell more even and to reduce the difference in temperature between the layers of the cell while lowering the pumping power [13]. In addition, they found that using heat sinks, such as two-layer microchannel heat sinks, produced the best temperature distribution while using much less pumping power. On the other hand, several studies [14] have used constructional theory to make stepwise varying-width microchannel (SVWMC) or multistage bifurcation microchannel (MSMC) heat sinks with the best heat transfer rates. Furthermore, numerical optimization was used to find the best location for the vertical splits inside the microchannel heat sink along the flow direction. A good cooling system is needed with many MJSC modules to increase their net power output and make them last longer [15]. A full three-dimensional thermal and electrical model was made to test how well the designs could lower the cell temperature and make the temperature more even. The findings showed that the traditional

jet impingement cooling scheme was not as good at cooling as the hybrid cooling schemes. Moreover, different coolants were used to test how to optimize the HCPVT system worked. The results showed that, when using water, the temperature of the solar cell achieved a uniform temperature distribution [16].

Nanofluids are made up of particles between 1 and 100 nm in size that are absorbed in a base fluid (water). Adding nanoparticles to a base fluid can make it much better at managing thermal heat. Additionally, the density, viscosity, and specific heat of the nanofluids relatively change [17]. So, a heat exchanger or an HCPV thermal system can make use of this in order to remove unrequired heat. A case study [18] focused on experimental and computational studies of PV cooling using different nanofluids, where nanoparticles were available in concentrations ranging from 0.05% to 10% by weight. The temperature dropped by 2% and thermal efficiency increased fourfold. In another study [11,19], a PV system was cooled with nanomaterials made of Al_2O_3 and Cu, which were mixed with ethylene glycol and water as the base fluid, and both the system performance and thermal conductivity increased by 11.82% and 0.74%, respectively. An additional numerical model was developed to look at how to improve a PVT system that uses Ag–water and Al–water nanofluids [20]. When Ag–water was used, the heat transfer rate increased by 43%, and the overall efficiency increased up to 4.5%.

Scientists studied an alumina-nanoparticle-based photovoltaic system dissolved in water. At a concentration ratio of 20 and a Reynolds number of 250, they determined that employing silicon carbide at a 4% volume fraction led to an increase of 15.05% in the electrical efficiency [21]. Moreover, a silicon solar cell configuration that was coupled to a silicon carbide microchannel heat sink was tested and subjected to a 15 suns concentration. The maximum temperature obtained was 167 °C, which is inadequate for HCPV applications; a maximum electrical efficiency of 19% was also obtained [22]. HCPVs can better convert energy than traditional photovoltaic (PV) panels, especially in places where the sun intensity is high. Multijunction (MJ) solar cells may be destroyed if the temperature surpasses 110 °C, as suggested by the manufacturer. The overall performance of an MJ solar cell with minichannel heat sinks and a high concentration ratio was studied to find a better way to cool down the cell. Experiments were performed to determine the heat transfer efficiencies of different fluids, and the model was processed by means of simulations as well [23]. One study improved the performance of a triangular-tube phase-change heat accumulator from three different perspectives. To begin, the authors compared three types of tubes: elliptical, square, and standard round tubes [24]. A triangle with equal sides was the optimum design for storing and releasing heat, according to the research findings.

On the other hand, researchers have tried different fin shapes to improve the ability of thermal collectors to collect heat. A case study with different fins on the bottom of the absorber plate was considered to improve the thermal performance in single-phase and double-phase solar thermal collectors. Moreover, researchers have studied how the fin's shape and design affect and handle heat dissipation [25,26]. In a different study [27], three types of molten salts were used as phase change materials (PCMs) in a computational study of how a three-stage cascaded latent heat thermal energy storage (LHTES) unit is filled and emptied. Each part of the machine was a vertical shell-and-tube heat exchanger filled with PCM and air on the shell side. During full charging and discharging, the liquid fraction, temperature, and total thermal energy of the PCMs, as well as the effects of the heat transfer fluid (HTF) intake temperature, were studied. The results indicated that cascading LHTES devices generate more heat and charge quicker at lower PCM melting temperatures. Cascaded LHTES systems are more adaptable than non-PCM LHTES systems because the PCM type can be selected [28]. Authors [29] examined what happens when an Al_2O_3–water nanofluid is used as a cooling fluid for multijunction solar cells in a Fresnel lens-based concentrated photovoltaic thermal CPVT system. They studied and compared both line focus and point focus, and the point-focus Fresnel lens was better at retaining the heat than the line-focus Fresnel lens in systems during operation [30]. Additionally, many researchers have studied CPV/T systems in the last 10 to 15 years [31–35].

These researchers have investigated at both theoretical and experimental aspects of models. The results of these studies show that hybrid CPV/T systems have special advantages for those in the energy business. These articles discuss CPV/T technology, including how solar collectors work, how they are designed, and various analyses of them. In one study, CPV/T collectors were broken down into subsystems to show how they work and affect the working of the whole system [36]. As the temperature and concentration ratio increases, the life cycle of CPV/T model lowered because the material goes under thermal stresses.

Researchers have also discussed the effects of these systems on the economy and the environment. The results showed that as the concentration ratio increased, the temperature at which the CPV/T system's ability to work reliably was negatively affected [37]. The cost and payback time are both influenced when the CPV/T works poorly. For instance, it costs 2.37 USD/W to run a CPV/T collector on electricity and 8.7 USD/W to run it on both electricity and heat. Levelized cost of energy analyses (LCOEs) were performed to determine the energy cost of a CPV/T system. MJ solar cells, heat exchangers, concentrators, pipelines, pumps, HTsF, and other parts are all part of the direct cost of a CPV/T system. The results showed that the LCOE for 30 MW of installed power is 0.043 USD/kWh and 0.016 USD/kWh for 120 MW [38]. Another study [39] investigated a new CPV/T hybrid systems composed of embedded GaInP/GaInAs/Ge cells and a point-focus Fresnel lens (PFFL), which was simulated in an indoor setting.

According to the literature, cooling is an excellent strategy for increasing MJSC module efficiency and ensuring energy security. One study focused on the effects of temperature on MJSC modules using an active cooling approach. The solar irradiance profile was measured for the entire day of 15 August 2022, and the value at 12:00 p.m. was taken into consideration for a simulation. Furthermore, the entire model, including the triple-junction solar cell, was designed in Solidworks software and a Fresnel lens was assumed to be at a 1500-sun concentration with 82% optical efficiency. This was followed by temperature profile creation in Ansys Workbench's steady-state thermal analyses (SSTA) domain. Additionally, thermal study was carried out using steady-state thermal analysis to assess the temperature profile, which was then connected with Ansys Fluent to determine the improved temperature profile. Overall, improvements in the electrical output and power profile of the MJSC were obtained with respect to a single mass flowrate (0.001 kg/s) throughout simulations under laminar flow boundary conditions.

Our study adds to the analysis of MJSC active cooling for the thermal management of the entire model for Pakistan's hot-temperature conditions. In addition, this research is valuable regarding the evaluation of the effect of nanoparticles in terms of nanofluids while considering the climate in Pakistan. Specifically, industrial realm of Lahore was taken into consideration. No such study was available for this specific location using nanofluids. This study will benefit academics and professionals in the field of renewable energy, particularly solar energy.

2. Methodology

2.1. Model Description

A MJSC was selected to investigate the impact of environmental parameters, especially during the early fall season on 15 August 2022 at around noon. Moreover, the parameters and equations related to our hypothesis were partially drawn from our earlier work [40]. In addition, the model was developed with Solidworks, which is shown in Figure 1, and its dimensions are provided in Table 1. We used 32 and 48 microchannels in this investigation for the 2- and 3-layer configurations, respectively, and only the 3-layer model is depicted from isometric, top, front, and rear views. There were a total of 6 layers including an MJSC, copper-1, Al_2O_3–ceramics, copper-2, thermal paste, and MCHS from top to bottom. The allowable temperature according by the manufacturer was below or equal to 110 °C, which was also taken from the literature. The temperature of the working fluid at the inlet was assumed to be 25 °C with a laminar flow boundary condition

at a single mass flow rate of 0.001 kg/s, and flow was assumed to be incompressible. A 1500-sun concentration was considered, and the heat-generating source was the top MJSC layer [41]. Natural convection and ambient temperature were considered to be applied on the top and sides of the model. The thermophysical properties of the various incorporated layers and nanofluids are shown in Tables 2 and 3. These values were estimated in terms of the numerical approach, which is described in the following section. Most values were obtained through case studies and datasheets given by manufacturers [42]. Additionally, this model was focusing on the effects of varying the volume concentrations of the nanoparticles, the thermophysical properties of the working fluids were considered at 5%, 10%, and 15% volume concentrations. Moreover, the material was taken as temperature-independent, and thermal resistances were neglected [43]. The thermophysical properties of the nanofluids were temperature-independent. Several studies have shown that the rate of cooling is faster if the working fluid has better thermophysical properties, especially a higher density. Other studies have shown that the best rates of heat transfer can be achieved by altering the values of thermal conductivity. Initially, steady-state thermal analysis (SSTA) was carried out obtain the temperature profile over a module where all associated boundary and environmental conditions were applied. Afterward, the coupling of SSTA and Ansys Fluent in Ansys Workbench was made to perform thermal management in terms of active cooling schemes. The element size during meshing, climatic conditions, and efficiency profiles are given in Table 4. The examined HCPV module had the following postulations that were selected for a three-dimensional computational fluid domain with conjugate heat transfer model:

1. The MJ solar cell was exposed to a 1500-suns concentration ratio and was considered a source of heat generation with a uniform solar flux [41,44].
2. Natural convection occurred on the top surfaces of all MJ solar cells, as well as the top copper layer and sides of the copper layers, ceramic material layer, thermal paste layer, and aluminum heat sinks (h = 22.78 W/(m^{2}K)).
3. Only the top surfaces of the MJ solar cell and the top copper layer were exposed to ambient radiations.
4. The reference electrical efficiency of the MJ solar cell was taken to be 42.35% at a concentration ratio of 1500 suns (1 sun = 805.00 W/m^2). Moreover, the solar cell had an antireflective coating, as specified in the manufacturer's data sheet [41].
5. The ambient temperature was 27 °C, which was site-dependent (Lahore, Pakistan).
6. We selected 15 August at noon for this investigation.
7. Only a single mass flow rate was adopted 0.001 kg/s at a fluid inlet temperature of 25 °C.
8. The material of the MJ solar cells was taken as temperature-independent and isotropic [45].
9. The thermal contact resistance between all the layers of the MJ solar cells and microchannel heat sinks was neglected [43].
10. Inside the microchannel heat sinks, coolant flow was considered to be constant, laminar, and incompressible.
11. Nanoparticle properties were temperature-independent, and he thermophysical properties are presented in Table 3.

Table 1. MJSC/T hybrid model description.

Layer	Length, mm	Width, mm	Thickness, mm
Germanium	10	10	0.19
Copper	25	25	0.25
Al$_2$O$_3$–Ceramic	30	30	0.32
Thermal Paste	25	25	0.3

Table 1. *Cont.*

Layer	Length, mm	Width, mm	Thickness, mm
Aluminum Heat Sinks	100	35	06
MCHS (2 and 3 Layers)	100	01	01
Gap between MC	-	01	01

Table 2. Thermophysical properties of different materials.

Layer	Thermal Conductivity, k (W/m·K)	Specific Heat, C_p (J/kg·K)	Density, ρ (kg/m^3)
Germanium	60	320	5323
Copper	400	385	8700
Al_2O_3–Ceramic	30	900	3900
Thermal Paste	10	800	4000
Aluminum Heat Sinks	202.6	87	2719

Table 3. Thermophysical properties of coolant for various volume fractions (VFs).

Nanofluid	Thermal Conductivity, k (W/m·K)	Specific Heat, C_p (J/kg·K)	Density, ρ (kg/m^3)	VF (φ_{np})
Al_2O_3–water	1.11	3590.55	1146.79	5%
SiO_2–water	1.16	3798.79	1058.29	
Al_2O_3–water	1.22	3134.78	1295.38	10%
SiO_2–water	1.32	3456.76	1118.38	
Al_2O_3–water	1.33	2772.81	1443.97	15%
SiO_2–water	1.47	3149.61	1178.47	

Table 4. Fluent solver, climatic conditions, efficiency profile, and material properties.

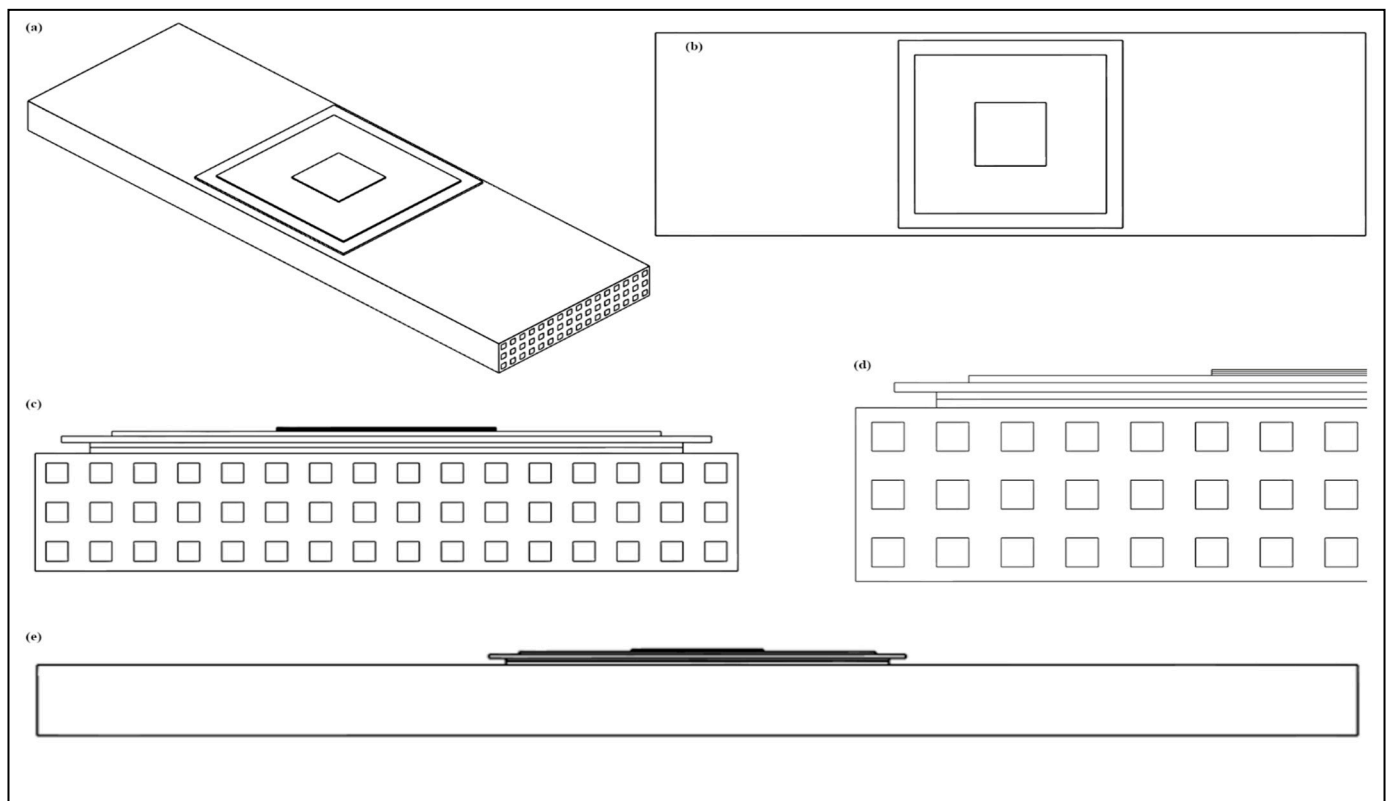| S. No.	Parameter	Value
1	Number of elements (meshing)	1,325,762
2	Heat induction (Q_h) W/m^2	575,399.78
3	Ambient remperature (T_a)	27
4	Emissivity of the germanium layer (ε_g)	0.9
5	Emissivity of the copper layer (ε_c)	0.05
6	Convective heat transfer coefficient (h_{conv})	22.78
7	Wind speed (m/h)	4.17
8	MJSC actual electrical efficiency	42.35%
9	MJSC efficiency without cooling	23.60%

Figure 1. Proposed MJSC/T 3-layer model: (**a**) isometric view, (**b**) top view, (**c**) front side view, (**d**) magnified front side view model, and (**e**) rear view.

2.2. HCPV-Module Layers

As the HCPV/T module contains different layers, the energy equation for each layer is:

$$\nabla \cdot (k_i \cdot \nabla T_i) + q_i = 0 \text{ and } i = 1, 2, \ldots 6 \tag{1}$$

where k_i, T_i, and q_i represent thermal conductivity, temperature, and solar flux absorption in the ith layer, respectively. The value of i was 1 to 6, representing each layer, which were the MJ solar cell, copper-1, Al_2O_3–ceramic, copper-2, thermal paste, and aluminum heat sink layers, respectively. The MJ solar cells layer was only a heat source in these layers. The heat source in this model in terms of absorbed solar flux was assigned to the energy equation of each MJ solar cell. The heat generation (q_{Ge}) in each MJ solar cell's layer was dependent on the direct normal irradiance (*DNI*), concentration ratio (*CR*), optical efficiency of a Fresnel lens (n_{opt}), and absorptivity of the germanium layer (α_{G_e}) [46]. This heat generation inside a germanium layer can be calculated with the following equation:

$$q_{Ge} = \frac{[1 - n_{MJSC}] DNI \cdot CR \cdot n_{opt} \cdot \alpha_{G_e} \cdot A}{V} \tag{2}$$

where n_{MJSC}, A, and V are the MJ solar cell's electrical efficiency, top surface area, and volume, respectively; $(1 - n_{MJSC})$ is the portion of absorbed solar irradiance that is converted into heat. Only direct normal irradiance was permitted in this research, and optical efficiency of a Fresnel lens was taken as ~81.5%. The electrical efficiency of an MJ solar cell varies according to the temperature on the cell's surface and can be formulated by the equation below [46]:

$$n_{MJSC} = \eta_{ref} \left[1 - \beta_{thermal} \cdot \left(T_{MJSC} - T_{ref}\right)\right] \tag{3}$$

where n_{MJSC} = 42.35% at a reference temperature of T_{ref} = 25 °C, and CR = 1500 suns [47]. The thermal coefficient $\beta_{thermal}$ increased by factor of 0.047% with a one-degree Kelvin increase in temperature, which was given by the manufacturer [46], but it can also be evaluated by employing the following expression [41]:

$$\beta_{thermal} = \frac{1}{\left(T_{MJSC,max} - T_{ref}\right)} \tag{4}$$

where $T_{MJSC,max}$ is a maximum temperature at which the efficiency of an MJSC becomes zero.

2.3. Governing Equations

In this section, mathematical methods are discussed, and most of the equations were obtained from previous work [40], and a few important equations are given.

2.3.1. Nanoparticles' Thermophysical Properties

The thermal conductivity (k_{nf}), specific heat ($C_{P,nf}$), and density (ρ_{nf}) of nanofluids at varying volume fractions (φ_{np}) and a particle size (D_{np}) of 20 nm were calculated as follows [48]:

$$k_{nf} = 1 + \varphi_{np}\left(1.0112\left(\frac{105.16251}{D_{np}}\right) - 0.0405 \cdot k_{np}\right) \cdot k_{bf} \tag{5}$$

$$C_{P,nf} = \frac{\varphi_{np} C_{P,np} \cdot \rho_{np} + (1 - \varphi_{np}) C_{P,bf} \cdot \rho_{bf}}{\rho_n} \tag{6}$$

$$\rho_{nf} = \varphi_{np} \rho_{np} + (1 - \varphi_{np}) \rho_{bf} \tag{7}$$

where k_{bf}, k_{np}, $C_{P,bf}$, $C_{P,np}$, and ρ_{bf}, ρ_{np} are the thermal conductivity, specific heat, and density of the base fluid (water) and nanoparticles, respectively. Their properties are displayed in Table 3.

2.3.2. Microchannel Heat Sinks

A fluid domain was coupled with the MCHS's aluminum substrate to study the flow behavior of a coolant by employing the heat conduction equation:

$$\nabla \cdot (k_i \cdot \nabla T_i) + q_i = 0 \tag{8}$$

where k_i and T_i are the thermal conductivity and temperature for layer i, respectively; q_i is the heat generation inside each cell of HCPV/T module, which can be expressed as Equation (2). In the rest of the layers, the heat generation was zero; hence, the equation is:

$$\nabla \cdot (k_i \cdot \nabla T_i) = 0 \tag{9}$$

As the fluid flow inside these MCHSs is steady, laminar, and incompressible, the governing equations for continuity, momentum and energy are as follows [41]:

$$\nabla \cdot (\rho_f \cdot \vec{V}) = 0 \tag{10}$$

$$\nabla \cdot (\rho_{nf} \cdot \vec{V}) = 0 \tag{11}$$

$$\vec{V} \cdot \nabla (\rho_f \cdot \vec{V}) = -\nabla P + \nabla (\mu_f \cdot \nabla \vec{V}) \tag{12}$$

$$\vec{V} \cdot \nabla (\rho_{nf} \cdot \vec{V}) = -\nabla P + \nabla (\mu_{nf} \cdot \nabla \vec{V}) \tag{13}$$

$$\vec{V} \cdot \nabla \left(\rho_f \cdot C_f \cdot T \right) = \nabla \cdot \left(k_f \cdot \nabla T \right) \tag{14}$$

$$\vec{V} \cdot \nabla \left(\rho_{nf} \cdot C_{nf} \cdot T \right) = \nabla \cdot \left(k_{nf} \cdot \nabla T \right) \tag{15}$$

where ρ_f, ρ_{nf}, μ_f, μ_{nf}, k_f, k_{nf}, C_f, and C_{nf}, are the density, dynamic viscosity, thermal conductivity, and specific heat for water and nanofluids, respectively. P and $\vec{V}$ are the pressure and velocity vector of a coolant, respectively. The hydraulic diameter can be estimated by using the following expression with the height and width of a microchannel.

$$D_h = \frac{2 \cdot W_{CH} \cdot H_{CH}}{W_{CH} + H_{CH}} = H_{CH} \tag{16}$$

For the Reynolds number of a working fluid, we can employ this formulation:

$$\mathrm{Re} = \frac{\rho_f \cdot v \cdot D_h}{\mu_f} \tag{17}$$

In order to determine the average Nusselt number and the overall thermal resistance for the MCHS, following expressions are used, where q_{Ge} is the solar heat flux (W/m^2); $T_{MCHS,avg}$ and $T_{FD,avg}$ are the average temperature of the microchannel heat sinks and fluid domain, respectively [49].

$$Nu_{avg} = \frac{q_{Ge} \cdot D_h}{\left(T_{MCHS,avg} - T_{FD,avg} \right) \cdot K_f} \tag{18}$$

$$R_{th} = \frac{T_{MCHS,max} - T_{f,in}}{q_{Ge}} \tag{19}$$

where $T_{MCHS,max}$ and $T_{f,in}$ are the maximum temperature of the microchannel heat sinks and inlet temperature of the working fluid, respectively. On the other hand, the convective heat transfer and electrical efficiency equations are, respectively, as follows:

$$h_{conv} = 5.82 + 4.07(V_w) \tag{20}$$

$$n_{MJSC} = \eta_{ref} \left[1 - \beta_{th} \cdot \left(T_{MJSC} - T_{ref} \right) \right] \tag{21}$$

where h_{conv} is the convective heat transfer coefficient due to the effect of wind speed (V_w; m/s), and n_{ref} = 42.35% is the reference efficiency at the reference temperature of T_{ref} = 25 °C and CR = 1500 suns [46].

3. Results and Discussion

3.1. Steady-State Thermal Analyses

In this part of the study, an MJSC with multiple layers were examined under the climatic conditions of Lahore, Pakistan, at noon on 15 August. In addition, 1500-sun CR was employed, and the results in terms of temperature contours are provided in Figure 2a,b. From steady-state thermal analysis, we found that the minimum, maximum, and average temperatures on the entire surface of the MJSC were 979 °C, 998 °C, and 991 °C, respectively. Moreover, in prior studies [50], it was observed that the maximum temperature of the MJSC layer increased to around 1000 °C when the CR increased to 1500 suns and above. At these temperature values, efficiency dropped to 23.6% from 42.35%, which was estimated to be a decrease of almost 44% under the set conditions. Temperature uniformity in this situation occurred at ~20 °C; at this temperature, the MJSC material does not deteriorate too much;

however, the reduction in the temperature is an overall concern that we assessed in the following study. The entire module exclusive of heat sinks is described below, while the complete hybrid unit was used to achieve the thermal management of the entire system.
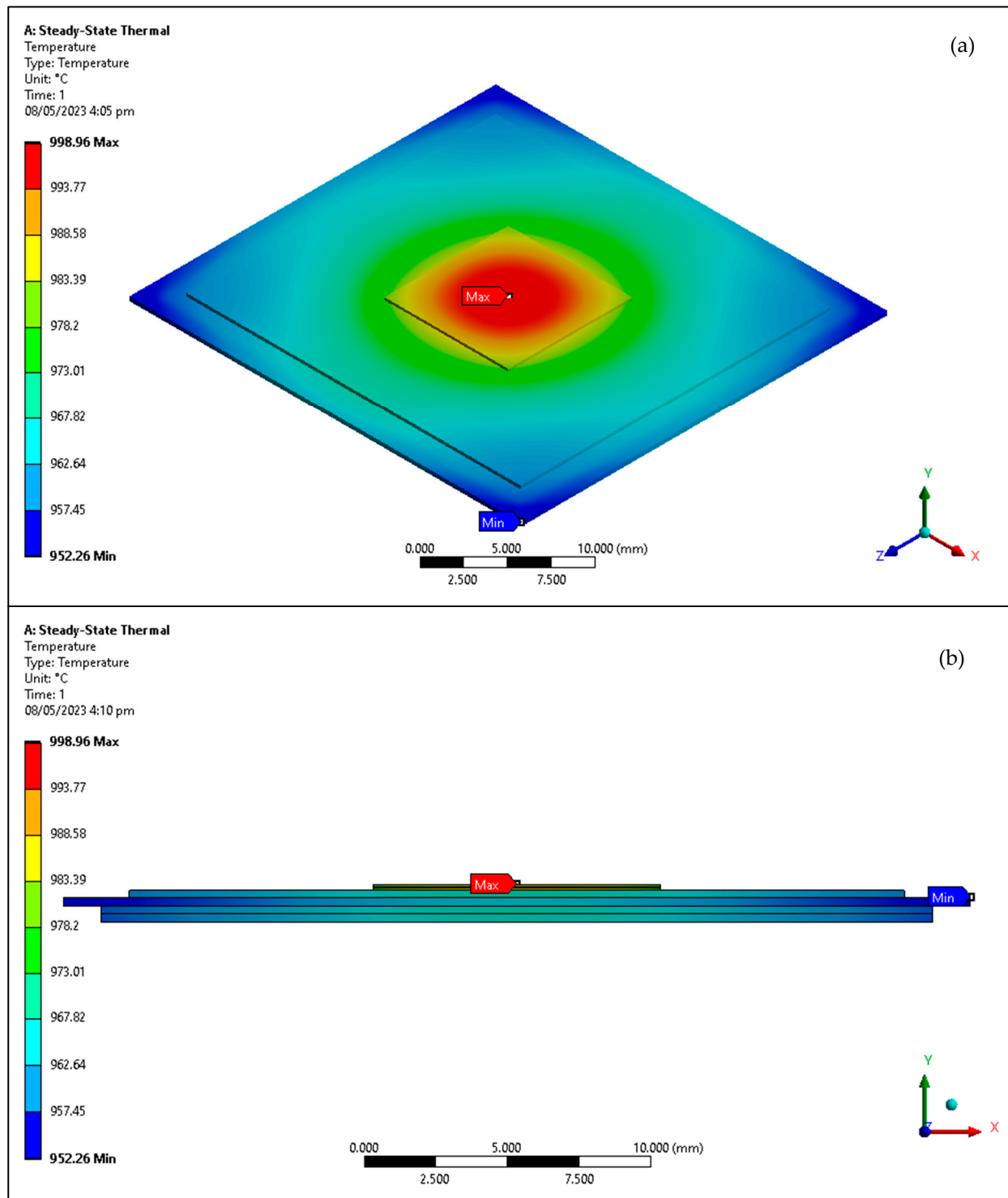

Figure 2. Temperature contours of MJSC with different layers without cooling (**a**) Isometric view & (**b**) Front view without channels.

3.2. SiO$_2$–Water vs. Al$_2$O$_3$–Water Temperature Contours at 15% Volume Fraction

We selected various volume fractions from 5% to 15% in this study, which is clearly shown in the figures. Simulations were performed only at a 0.001 kg/s mass flow rate.

In Figure 3, the temperature profile of the MJSC only is shown, where comparative and pictographically contours are shown for SiO_2–water and Al_2O_3–water-based nanofluids with two- and three-layer microchannels assemblies. Moreover, only the contours of the MJSC at 15% volume fraction can be seen, while the rest of the contours are displayed in the figures below. In Figure 3, the minimum, average and maximum temperatures of the MJSC are 59.141 °C, 88.175 °C, and 106.46 °C; and 60.368 °C, 89.631 °C, and 108 °C for the SiO_2–water and Al_2O_3–water nanofluids, respectively, with two layers of MCHS. On the other hand, regarding three layers of MCHS, the temperature was 34.818 °C, 44.496 °C, and 51.291 °C; and 35.015 °C, 44.722 °C, and 51.536 °C for SiO_2–water and Al_2O_3–water nanofluids, respectively. On the other hand, the complete model equipped with MJSC, and additional layers inclusive of MCHS can be seen in Figure 4, where two and three layers are illustrated, as well as the temperature distribution, throughout a complete model, which indicates that the high-temperature distribution appeared on the heating source (MJSC) inclusive of the complete model according to CFD analysis. The temperature range was quite different between the three- and two-layer systems, being 25–108 °C for two layers and 25–52 °C for three layers. In Figure 5, the streams of working fluids are shown for a 15% volume concentration under laminar flow boundary conditions. Moreover, it can be seen from Figure 5 that at a 0.001 kg/s mass flow rate, the maximum temperature of the coolant at the outlet was 54.95 °C, 56.65 °C, 32.75 °C, and 33.05 °C for two layers of SiO_2–water, two layers of Al_2O_3–water, three layers of SiO_2–water, and three layers of Al_2O_3–water, respectively. The overall temperature of the working fluid that we found by using the area-weighted average method inside a fluent solver was 30.47 °C, 31.83 °C, 25 °C, and 25 °C for two layers of SiO_2–water, two layers of Al_2O_3–water, three layers of SiO_2–water, and three layers of Al_2O_3–water, respectively. The results of the temperature profiles are given in the following section in the form of line graphs.
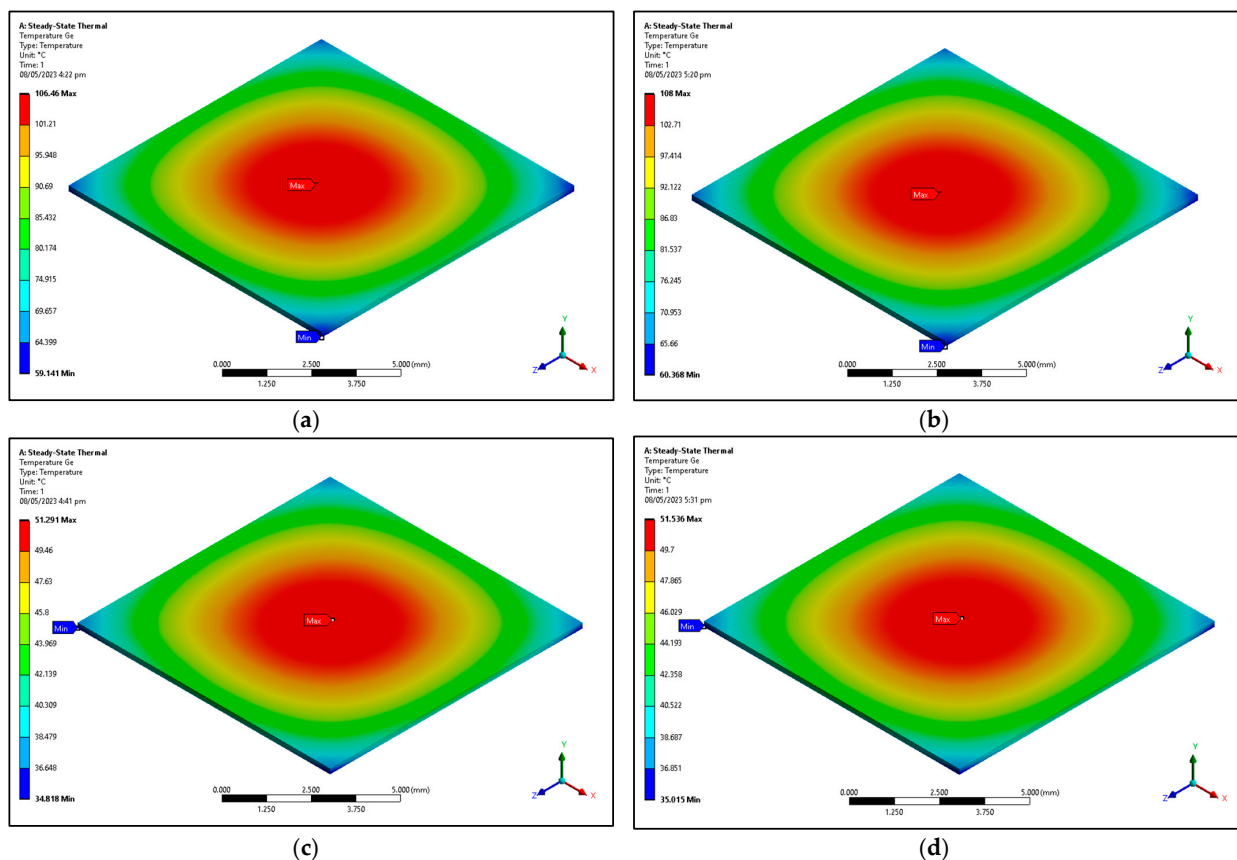

Figure 3. (**a**) MJSC layer with 2 layers of MCHS under SiO_2–water coolant, (**b**) MJSC layer with 2 layers of MCHS under Al_2O_3–water coolant, (**c**) MJSC layer with 3 layers of MCHS under SiO_2–water coolant, and (**d**) MJSC layer with 3 layers of MCHS under Al_2O_3–water coolant.
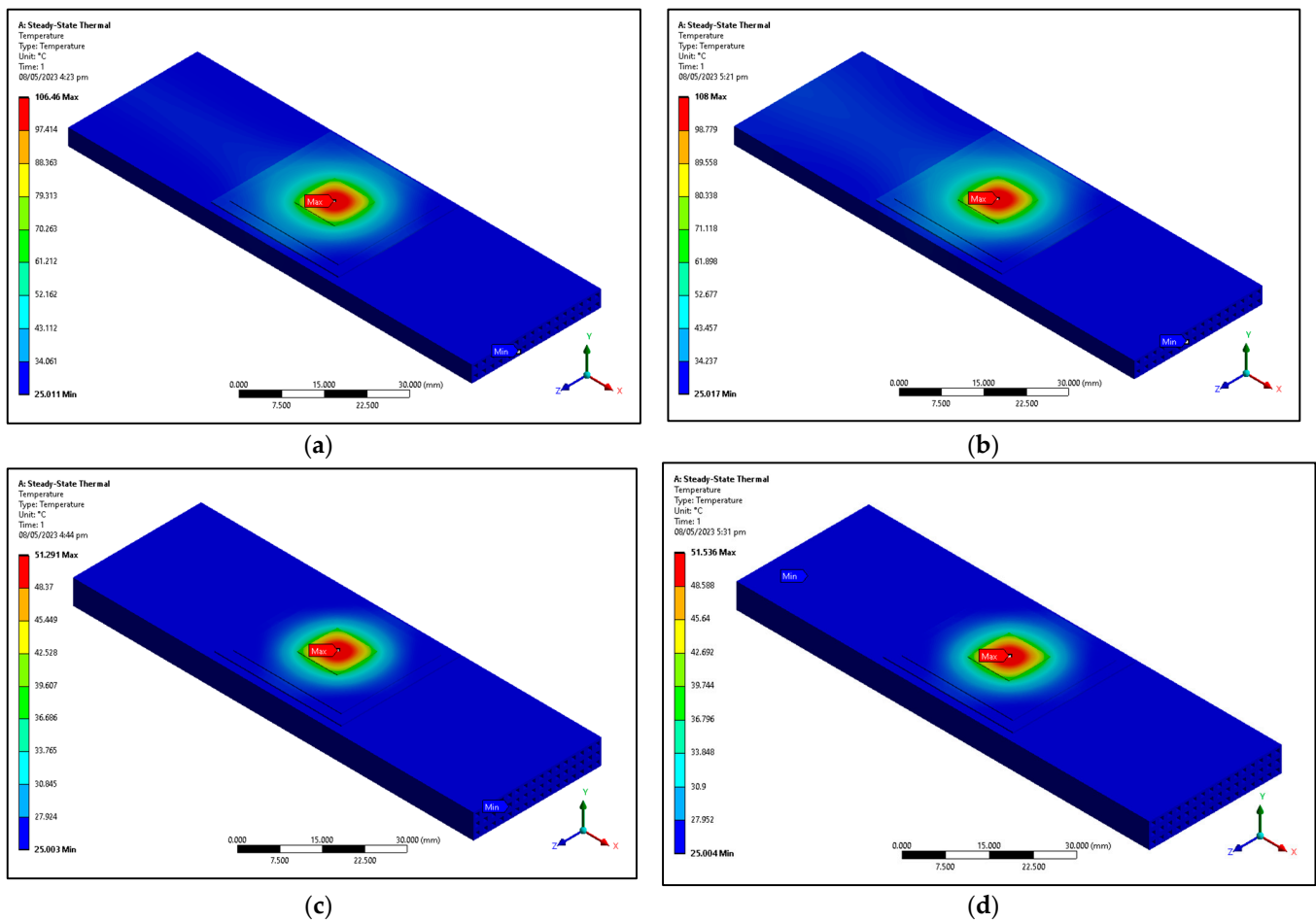
(a)　　　　　　　　　　　　　　　(b)

(c)　　　　　　　　　　　　　　　(d)

Figure 4. (**a**) Complete MJSC unit with 2 layers of MCHS under SiO_2–water coolant, (**b**) complete MJSC unit with 2 layers of MCHS under Al_2O_3–water coolant, (**c**) MJSC layer with 3 layers of MCHS under SiO_2–water coolant, and (**d**) MJSC layer with 3 layers of MCHS under Al_2O_3–water coolant.
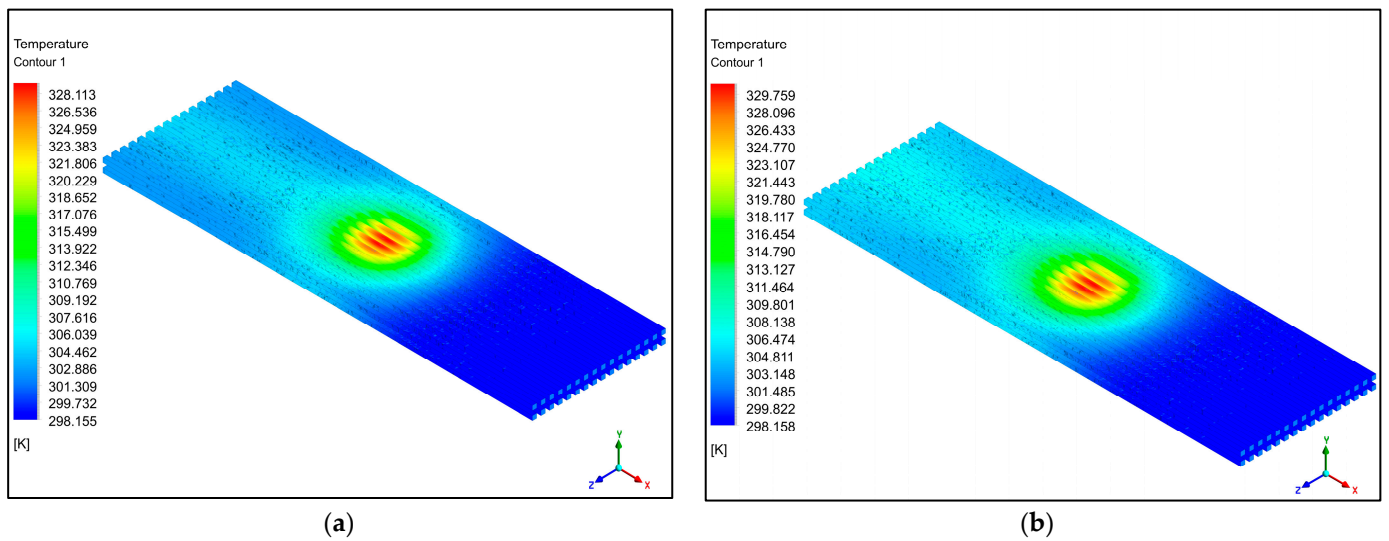

(a)　　　　　　　　　　　　　　　(b)

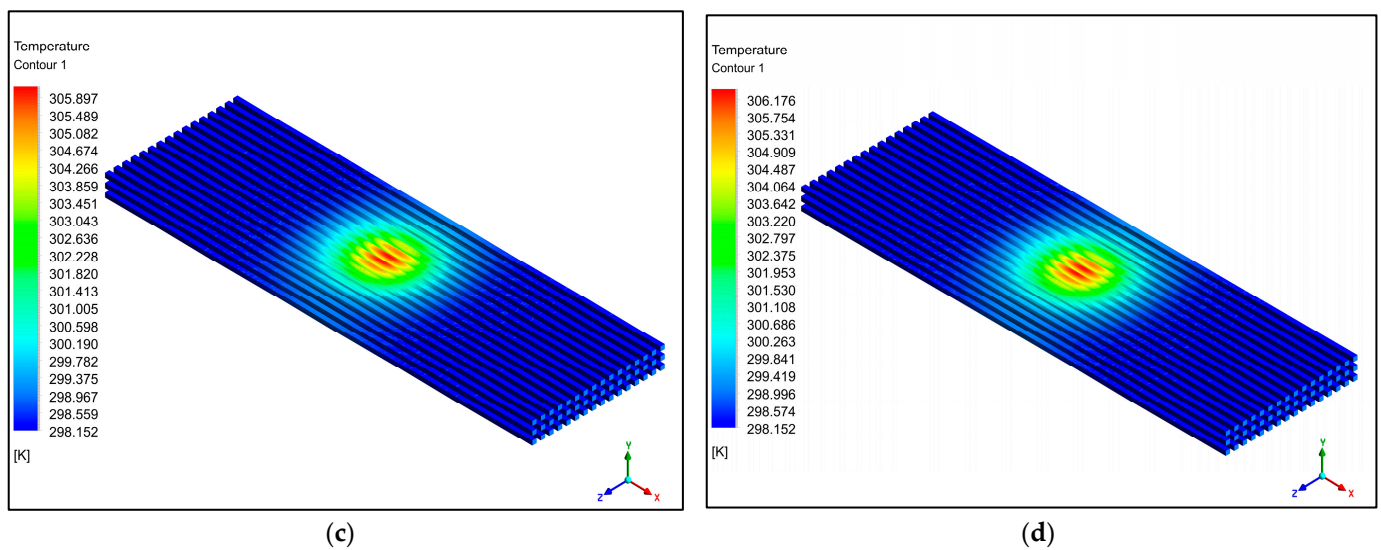**Figure 5.** *Cont.*

(c)

(d)

Figure 5. (**a**) Temperature contours of 2-layer MCHS under SiO_2–water coolant, (**b**) 2-layer MCHS under Al_2O_3–water coolant, (**c**) 3-layer MCHS under SiO_2–water coolant, and (**d**) 3-layer of MCHS under Al_2O_3–water coolant.

3.3. Temperature Profiles

This section deals with all temperature-associated studies, with results presented in graphical form. Figure 6 shows the minimum temperature achieved during CFD simulations with two nanofluids, namely, SiO_2–water and Al_2O_3–water, at a 0.001 kg/s mass flow rate. In part (a), the results for two-layer MCHS indicate that SiO_2–water nanofluids achieved a lower temperature than Al_2O_3–water nanofluids. At a 5% volume fraction, the minimum temperature on the MJSC surface was found to be 60.8 °C under SiO_2–water compared with the 61.4 °C under the Al_2O_3–water working fluid. In addition, it was found that the temperature increased as the volume concentration increased from 5% to 15%. Moreover, the difference in the temperature at the highest volume concentration was almost 2 °C for two-layer MCHS. Similarly, for three-layer MCHS, the results in (b) show that the difference in temperature for both of the working fluids remained close throughout all the simulations at various volume concentrations. In other words, three-layer MCHS integrated with MJSC was found to be efficient regarding the minimum temperature profile. The maximum temperature in Figure 7 again shows the efficient results achieved with SiO_2–water nanofluid compared with those of Al_2O_3–water. Moreover, the lower maximum temperature values were maintained with the increase in volume concentration. For the two-layer assembly, the efficient and allowable maximum temperature achieved with SiO_2–water at 15% volume concentration was around 106.5 °C, whereas for the three-layer configuration, the temperature was achieved at almost 51 °C with the same working fluid at the same volume concentration. Secondly, the three-layers assembly had an efficient impact on the life span of the MJSC due to the maximum temperature being below 110 °C. Regarding the average temperature, Figure 8 shows that the temperature profile decreased with increasing volume concentration of the nanoparticles. At 5% volume concentration, the optimum average temperature was just above and below 90 °C for the Al_2O_3–water and SiO_2–water, respectively, in the two-layer case. Moreover, at the 15% volume concentration, again the difference in values remained at around 2 °C. On the other hand, for the three-layer case, overall, the average temperature profile was just below 45.5 °C, which was found to be favorable for the life of the MJSC material. At this stage, it was found that at a 15% volume concentration and 0.001 kg/s mass flow rate, the values were optimum for all simulations, and the best efficiency of the MJSC was achieved by using SiO_2–water nanofluid with the three-layer MJSC/T model. In terms of temperature uniformity, Figure 9 depicts that when using two-layer assemblies, although the results were closer, the trend for

the SiO$_2$–water nanofluid was positive: the values decreased with the increase in volume concentration, whereas for the Al$_2$O$_3$–water nanofluid, the values gradually increased with the increase in volume concentration. For three layers, the temperature uniformity ranged between 16.45 °C and 16.65 °C for all the simulations; nonetheless, the values of SiO$_2$–water were optimal (16.47 °C) at a 15% volume concentration. Finally, regarding the outlet temperature of the working fluid in the case of the two-layer configurations, the highest outlet temperature (31.83 °C) was achieved with Al$_2$O$_3$–water at a 15% volume concentration, whereas the minimum outlet temperature of the working fluid stream was found to be 29.53 °C at a 5% volume concentration. The three-layer results are nearer to the intake temperature of the working fluid, which means 25 °C throughout all the simulations at 5%, 10%, and 15% volume concentrations for both of the nanofluids. In addition, it can be seen that the working fluid with an optimum effect on the average MJSC temperature had a lower-temperature outlet stream. On the other hand, the working fluid that contributed the least toward the thermal management of the MJSC had the maximum temperature for the outgoing coolant stream at the outlet, which is shown in Figure 10.
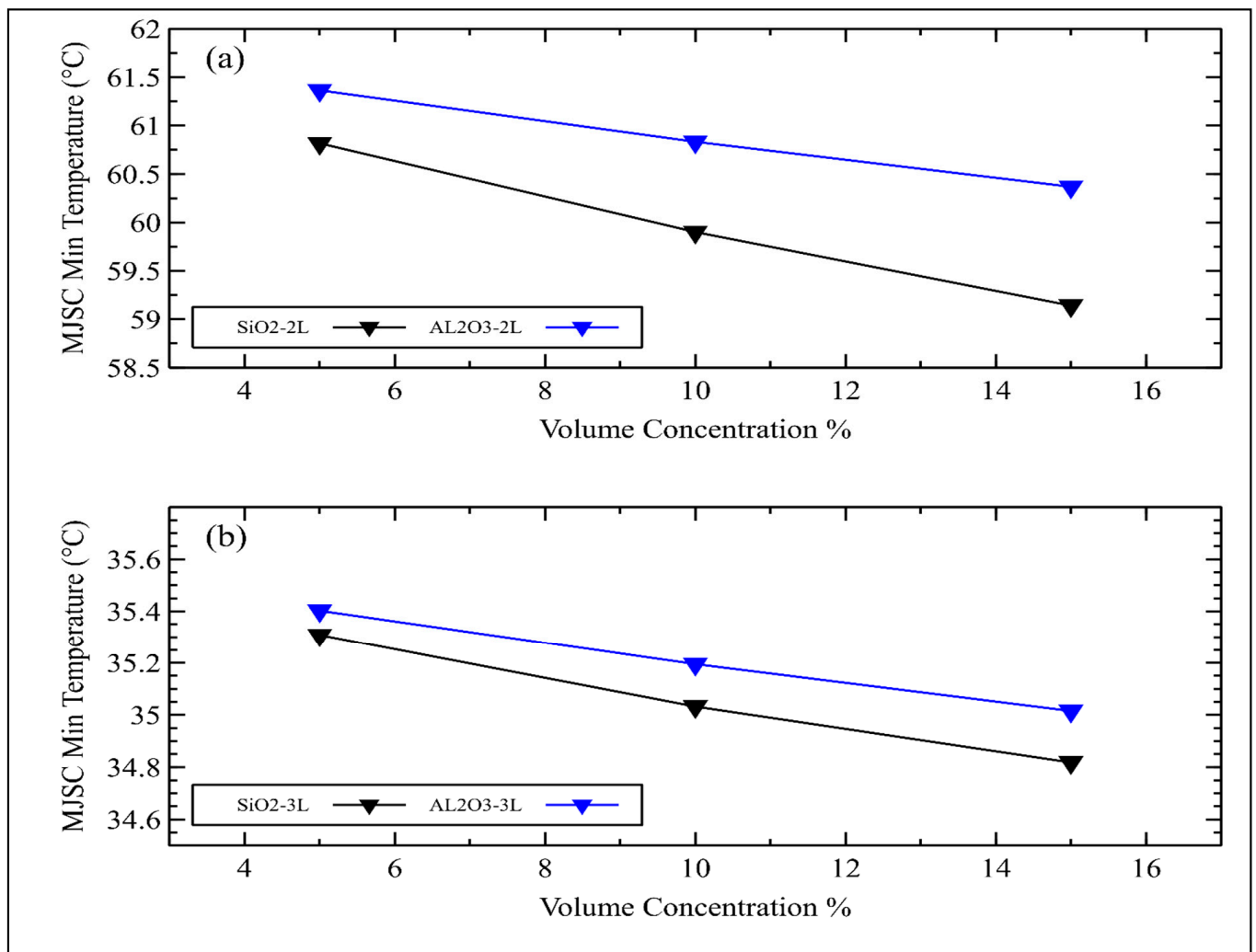

Figure 6. (**a**) Minimum temperature of MJSC with SiO$_2$–water or Al$_2$O$_3$–water coolant integrated with 2 layers of MCHS and (**b**) MJSC with SiO$_2$–water and Al$_2$O$_3$–water coolants integrated with 3 layers of MCHS.
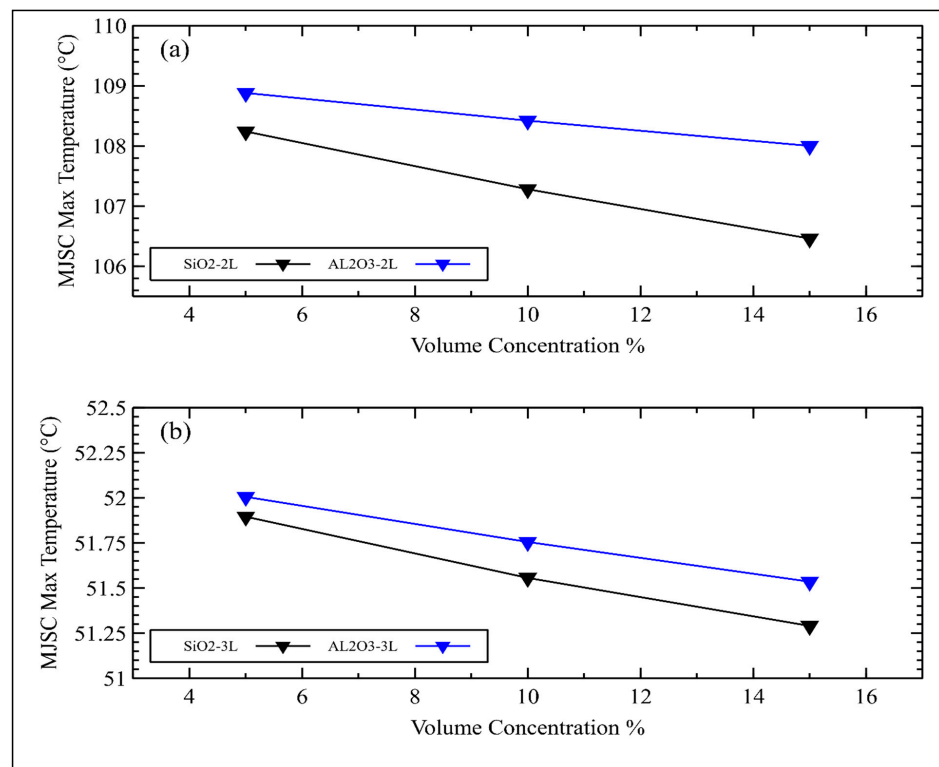
Figure 7. (**a**) Maximum temperature of MJSC with SiO$_2$–water or Al$_2$O$_3$–water coolant integrated with 2 layers of MCHS and (**b**) MJSC with SiO$_2$–water or Al$_2$O$_3$–water coolant integrated with 3 layers of MCHS.
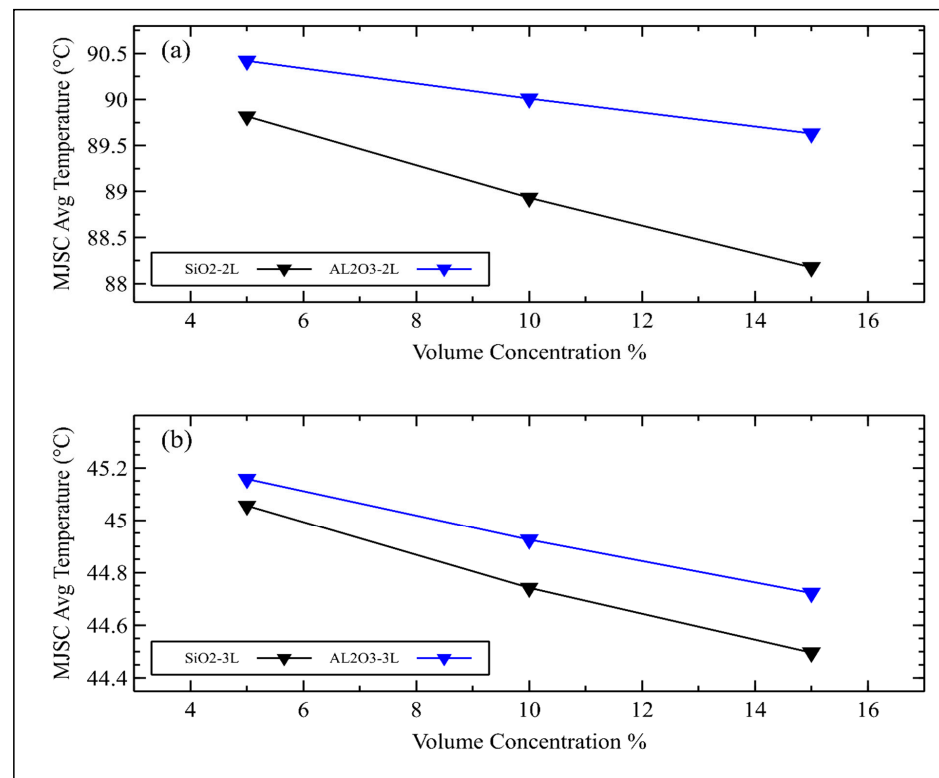

Figure 8. (**a**) Average temperature of MJSC with SiO$_2$–water or Al$_2$O$_3$–water coolant integrated with 2 layers of MCHS and (**b**) MJSC with SiO$_2$–water or Al$_2$O$_3$–water coolant integrated with 3 layers of MCHS.

Figure 9. (**a**) Temperature uniformity of MJSC with SiO_2–water or Al_2O_3–water coolant integrated with 2 layers of MCHS and (**b**) MJSC with SiO_2–water or Al_2O_3–water coolants integrated with 3 layers of MCHS.
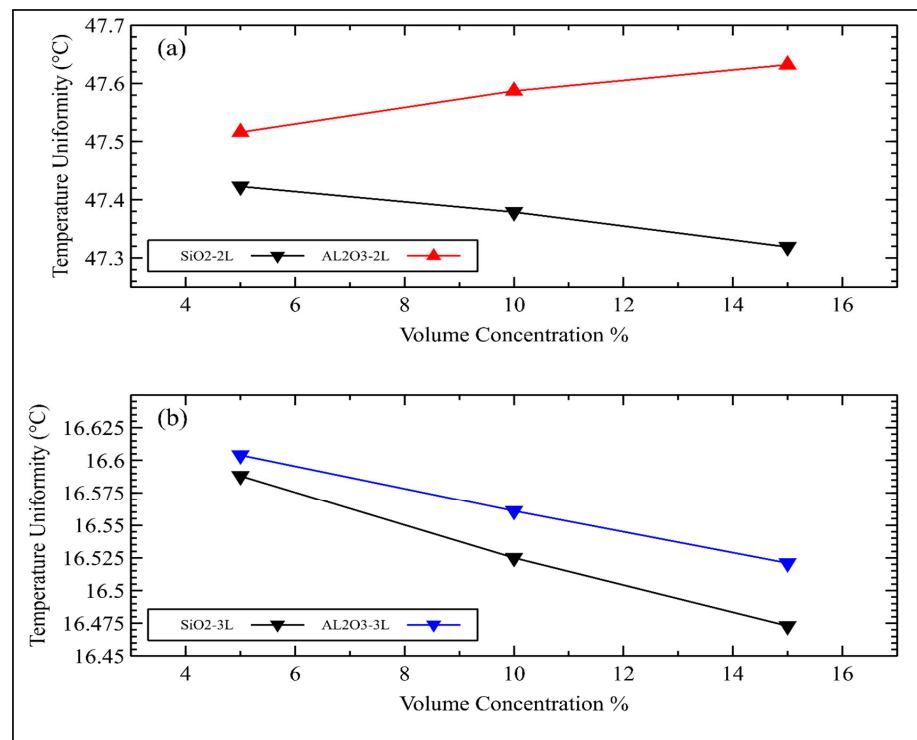

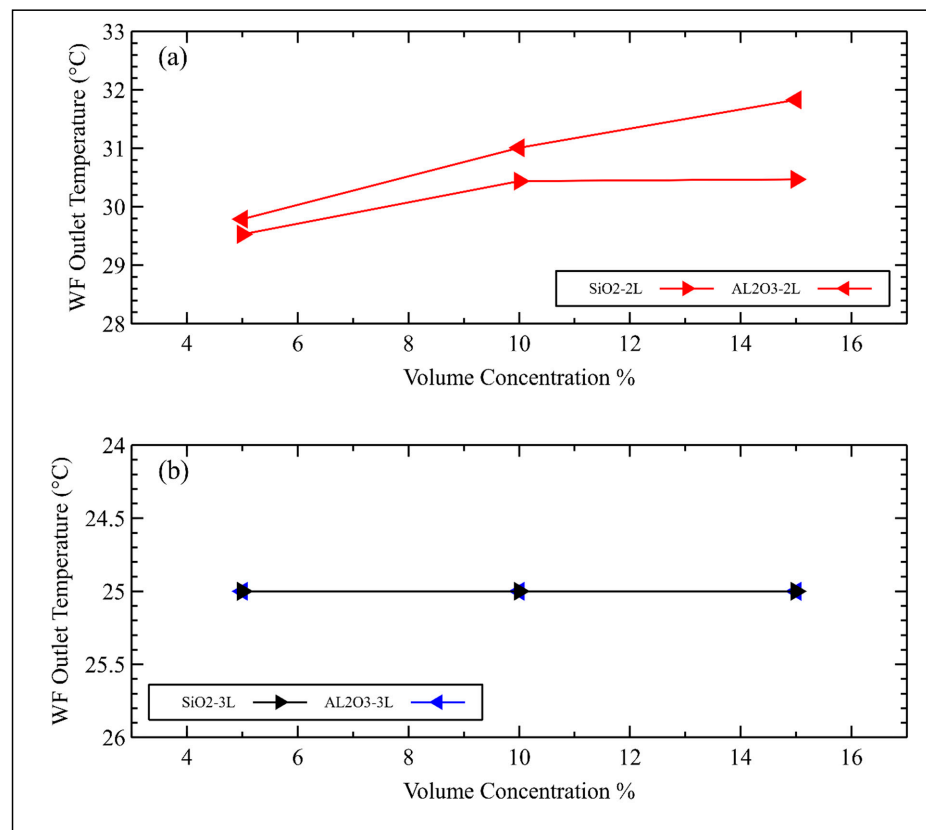**Figure 10.** (**a**) Working fluid outlet temperature of MJSC with SiO_2–water or Al_2O_3–water coolant integrated with 2 layers of MCHS and (**b**) MJSC with SiO_2–water or Al_2O_3–water coolant integrated with 3 layers of MCHS.

3.4. Electrical Efficiency Curves

In this last section of the paper, electrical efficiency improvement curves are illustrated for better comprehension of the case study at different volume concentrations, for two- and three-layer configurations at the same mass flow rate of 0.001 kg/s. It can be seen that without cooling off the entire model, the efficiency was around 23%. Examining Figure 11 shows that the efficiency of the MJSC increased as the volume concentration increased. Moreover, Figure 11a, for two layers, shows that the optimum electrical efficiency as maintained at 41.09% by the SiO_2–water nanofluid at a 15% volume concentration. The Al_2O_3–water working fluid attained a 41.06% benchmark under the same conditions. Regarding the values at lower concentrations, the minimum electrical efficiency values were found to be almost 41.06% and 41.05% for the SiO_2–water and Al_2O_3–water coolants, respectively. In the second part of Figure 11b, the results for the three-layer configurations are shown, indicating that the maximum values were again obtained by the SiO_2–water coolant. In addition, the minimum and maximum efficiency values for SiO_2–water and Al_2O_3–water were 41.95% and 41.95%, and 41.97% and 41.96%, respectively. Finally, the improvement in efficiency can be observed in Figure 12, where the efficiency increased from 23% in the no-cooling case to 41.97% (highest cooling). The efficiency increased by 17.47% to 17.5% with the addition of SiO_2–water coolant in the two-layer configuration, while the Al_2O_3–water working fluid contributed between 17.46% and 17.47% to the efficiency for volume concentrations from 5% to 15%. In (b), for the three-layers MCHS modeling, the MJSC added 18.36%, 18.365%, and 18.37% efficiency for the 5%, 10%, and 15% volume fractions, respectively, with the SiO_2–water nanofluid. Regarding Al_2O_3-water working fluid, the additions to efficiency were below 18.36%, above 18.365%, and 18.37% for the 5%, 10%, and 15% volume fractions, respectively. Overall, the values obtained with the SiO_2–water nanofluid were superior to those obtained with the Al_2O_3–water nanofluid in all cases irrespective of the outlet temperature of the coolant.
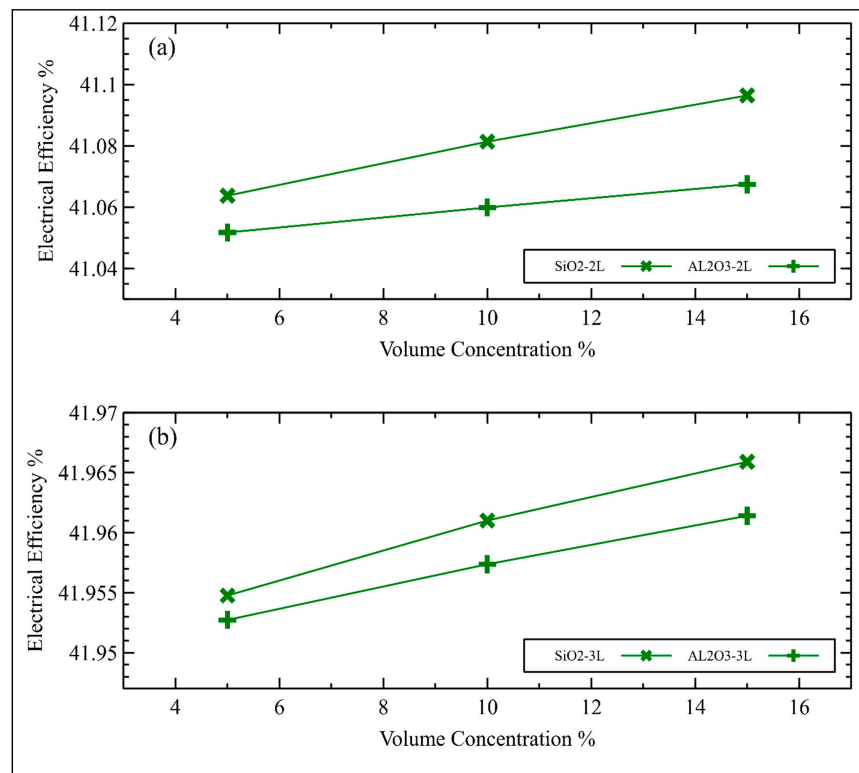

Figure 11. (**a**) Electrical efficiency of MJSC with SiO_2–water or Al_2O_3–water coolants integrated with 2 layers of MCHS and (**b**) MJSC with SiO_2–water or Al_2O_3-water coolant integrated with 3 layers of MCHS.
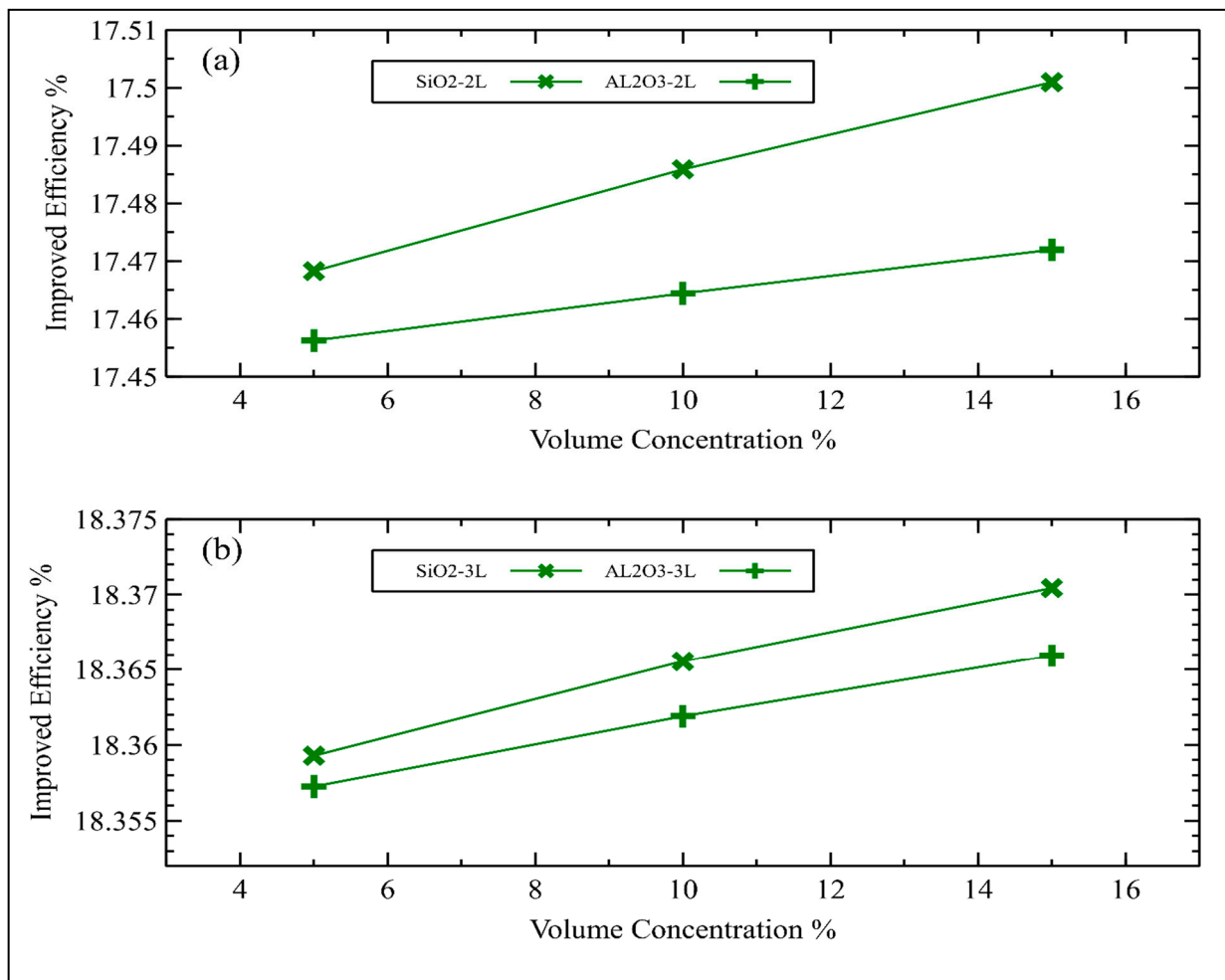
Figure 12. (**a**) Improvement in electrical efficiency of MJSC with SiO$_2$–water or Al$_2$O$_3$–water coolant integrated with 2 layers of MCHS and (**b**) MJSC with SiO$_2$–water or Al$_2$O$_3$–water coolants integrated with 3 layers of MCHS.

4. Conclusions

In this research, the triple-junction solar cell was taken into consideration, and a 3D model including different layers and microchannel heat sinks (MHSs) was developed in Solidworks 2022. Moreover, the areas of the MJSC and Fresnel lens were found to be 10 mm × 10 mm (modeled) and 387 mm × 387 mm (assumed), respectively. So, the Fresnel lens with 1500 suns and ~81.5% optical efficiency were selected for 15 August 2022 during solar noon at an industrial location in Lahore, Pakistan. The rest of the layers that were designed included copper-1, Al$_2$O$_3$–ceramics, copper-2, thermal paste, and an MHS with two or three layers at the bottom. Some of the following findings were obtained from the study:

- The incident flux while working on this model was 805 W/m^2 for the direct radiation.
- The efficiency of the MJSC after SSTA was found to be 23% instead of 42.35% at the set concentration ratio.
- In order to restore the lost electrical output as a drawback of a concentrated MJSC system, an active cooling option was considered at a 0.001 kg/s mass flow rate only.
- Two nanofluids, namely, SiO$_2$–water and Al$_2$O$_3$–water, were carefully chosen.
- For thermal management, the coupling of SSTA and Ansys Fluent was made using Ansys Workbench.
- The results of this study were produced in the form of SSTA output, temperature contours, temperature profiles, and electrical outputs.

- In SSTA, the average temperature of 991 °C was observed, and the efficiency dropped to 23% with a temperature uniformity of around 20 °C for the mentioned boundary and climatic conditions.
- Temperature contours emphasized the optimum results achieved by the SiO_2–water nanofluid throughout all the simulations.
- Both working fluids achieved an allowable maximum temperature below 110 °C for both MCHS arrangements.
- The minimum, maximum, and average temperatures of the MJSC with the SiO_2–water working fluid were efficient at about 34.9 °C, 51.3 °C, and 44.5 °C, respectively, with the three-layer MCHS assembly at a 15% volume concentration.
- The temperature uniformity of the SiO_2–water working fluid at a 15% volume fraction was found to be 16.47 °C.
- The maximum outlet temperature of the working fluid of the Al_2O_3–water nanofluid at all volume concentrations ranged from 29.53 °C to 31.83 °C. For the three-layer configuration, the input and output temperatures of the working fluid were found to be identical.
- The maximum electrical efficiency of the MJSC was 41.97% and 41.95% for SiO_2–water and Al_2O_3–water coolants, respectively, at a 15% volume concentration.
- SiO_2–water was found to be an optimum coolant compared with Al_2O_3–water regarding efficiency improvement, while Al_2O_3–water showed a better ability to have a maximum outlet temperature.

Author Contributions: Conceptualization, M.A. (Muhammad Asim) and M.H.T.; methodology, M.H.T.; software, M.M.A.; validation, A.K. (Ammara Kanwal); formal analysis, M.A. (Muhammad Amjad); investigation, A.A.; data curation, M.H.T.; writing—original draft preparation, M.A. (Muhammad Asim) and M.H.T.; writing—review and editing, M.A. (Muhammad Amjad), M.H.T., A.K. (Ammara Kanwal), A.K. (Aamna Khalid), F.R., M.M.A., M.A.K.; supervision, M.A. (Muhammad Asim); funding acquisition, F.R. All authors have read and agreed to the published version of the manuscript.

Nomenclature

HCTJSC	Highly Concentrated Triple-Junction Solar Cells
MCHS	Microchannel Heat Sinks
CR	Concentration Ratio
PCM	Phase Change Material
LHTES	Latent Heat Thermal Energy Storage
HTF	Heat Transfer Fluid
LCOE	Levelized Costs of Energy
GaInP	Gallium Indium Phosphide
GaInAs	Gallium Indium Arsenide
Ge	Germanium
PFFL	Point Focus Fresnel Lens
φ_{np}	Volume Fraction of Nanoparticles
D_{np}	Particle Size
K	Thermal Conductivity of Nanofluids
K_w	Thermal Conductivity of Water
K_{np}	Thermal Conductivity of Nanoparticles
Cp	Specific Heat of Nanofluids
Cp_w	Specific Heat of Water
Cp_{np}	Specific Heat of Nanoparticles
ρ	Density of Nanofluids
ρ_w	Density of Water

ρ_{np}	Density of Nanoparticles
Q_h	Heat Induction
T_a	Ambient Temperature
ε_g	Emissivity of the germanium layer
ε_c	Emissivity of the copper layer
h_{conv}	Convective Heat Transfer Coefficient
V_w	Wind Velocity (m/s)
n_{MJSC}	New Efficiency of MJSC
η_{ref}	Reference Efficiency
β_{th}	Thermal Coefficient
T_{MJSC}	Temperature of MJSC
T_{ref}	Reference Temperature

References

1. Tahir, Z.R.; Kanwal, A.; Asim, M.; Bilal, M.; Abdullah, M.; Saleem, S.; Mujtaba, M.A.; Veza, I.; Mousa, M.; Kalam, M.A. Effect of Temperature and Wind Speed on Efficiency of Five Photovoltaic Module Technologies for Different Climatic Zones. *Sustainability* **2022**, *14*, 15810. [CrossRef]
2. Tang, W.; Li, J.; Lu, J.; Sheng, K.; Wu, Z.; Li, X. Thermal management of GaN HEMT devices using subcooled flow boiling in an embedded manifold microchannel heat sink. *Appl. Therm. Eng.* **2023**, *225*, 120174. [CrossRef]
3. Saleem, M.W.; Abbas, A.; Asim, M.; Uddin, G.M.; Chaudhary, T.N.; Ullah, A. Design and cost estimation of solar powered reverse osmosis desalination system. *Adv. Mech. Eng.* **2021**, *13*, 16878140211029090. [CrossRef]
4. Asim, M.; Qamar, A.; Kanwal, A.; Uddin, G.M.; Abbas, M.M.; Farooq, M.; Kalam, M.A.; Mousa, M.; Shahapurkar, K. Opportunities and Challenges for Renewable Energy Utilization in Pakistan. *Sustainability* **2022**, *14*, 10947. [CrossRef]
5. Sarwar, J.; Shad, M.R.; Hasnain, A.; Ali, F.; Kakosimos, K.E.; Ghosh, A. Performance analysis and comparison of a concentrated photovoltaic system with different phase change materials. *Energies* **2021**, *14*, 2911. [CrossRef]
6. Alzahrani, M.M.; Roy, A.; Sundaram, S.; Mallick, T.K. Investigation of Thermal Stress Arising in a Graphene Neutral Density Filter for Concentrated Photovoltaic System. *Energies* **2021**, *14*, 3515. [CrossRef]
7. Usman, M.; Jamil, M.K.; Riaz, F.; Hussain, H.; Hussain, G.; Shah, M.H.; Qyyum, M.A.; Salman, C.A.; Lee, M. Refining and Reuse of Waste Lube Oil in SI Engines: A Novel Approach for a Sustainable Environment. *Energies* **2021**, *14*, 2937. [CrossRef]
8. Shahid, M.I.; Asim, M.; Farhan, M.; Sheikh, M.F.; Ashraf, M.U.; Arshad, H.; Alghamdi, A.; Alshahrani, A.S.; Bahaddad, A.A.; Almarhabi, K.A. Design and performance analysis of salinity gradient solar pond under different climatic and soil conditions. *PLoS ONE* **2023**, *18*, e0279311. [CrossRef]
9. Elsheniti, M.B.; AlRabiah, A.; Al-Ansary, H.; Almutairi, Z.; Orfi, J.; El-Leathy, A. Performance Assessment of an Ice-Production Hybrid Solar CPV/T System Combining Both Adsorption and Vapor-Compression Refrigeration Systems. *Sustainability* **2023**, *15*, 3711. [CrossRef]
10. Tahir, Z.u.R.; Azhar, M.; Blanc, P.; Asim, M.; Imran, S.; Hayat, N.; Shahid, H.; Ali, H. The evaluation of reanalysis and analysis products of solar radiation for Sindh province, Pakistan. *Renew. Energy* **2020**, *145*, 347–362. [CrossRef]
11. Zahid, I.; Farhan, M.; Farooq, M.; Asim, M.; Imran, M. Experimental investigation for thermal performance enhancement of various heat sinks using Al_2O_3 NePCM for cooling of electronic devices. *Case Stud. Therm. Eng.* **2023**, *41*, 102553. [CrossRef]
12. Xia, Y.; Chen, L.; Luo, J.; Tao, W. Numerical investigation of microchannel heat sinks with different inlets and outlets based on topology optimization. *Appl. Energy* **2023**, *330*, 120335. [CrossRef]
13. Ashraf, W.M.; Rafique, Y.; Uddin, G.M.; Riaz, F.; Asim, M.; Farooq, M.; Hussain, A.; Salman, C.A. Artificial intelligence based operational strategy development and implementation for vibration reduction of a supercritical steam turbine shaft bearing. *Alex. Eng. J.* **2022**, *61*, 1864–1880. [CrossRef]
14. Abo-Zahhad, E.M.; Ookawara, S.; Radwan, A.; Elkady, M.; El-Shazly, A. Optimization of stepwise varying width microchannel heat sink for high heat flux applications. *Case Stud. Therm. Eng.* **2020**, *18*, 100587. [CrossRef]
15. Yu, C.; Zhu, X.; Li, Z.; Ma, Y.; Yang, M.; Zhang, H. Optimization of elliptical pin-fin microchannel heat sink based on artificial neural network. *Int. J. Heat Mass Transf.* **2023**, *205*, 123928. [CrossRef]
16. Sabry, M.; Lashin, A. Performance of a Heat-Pipe Cooled Concentrated Photovoltaic/Thermoelectric Hybrid System. *Energies* **2023**, *16*, 1438. [CrossRef]
17. Jowkar, S.; Shen, X.; Olyaei, G.; Morad, M.R.; Zeraatkardevin, A. Numerical analysis in thermal management of high concentrated photovoltaic systems with spray cooling approach: A comprehensive parametric study. *Sol. Energy* **2023**, *250*, 150–167. [CrossRef]
18. Ammasi, A.; Iruthayaraj, R.; Munusamy, A.P.; Shkir, M. Molecular engineering on D-π-A organic dyes with flavone-based different acceptors for highly efficient dye-sensitized solar cells using experimental and computational study. *J. Mol. Model.* **2023**, *29*, 45. [CrossRef]
19. Moghaddam, M.H.; Karami, M. Thermohydraulic optimization of artificial roughness in photovoltaic-thermal (PVT) system using genetic algorithm. *J. Build. Eng.* **2023**, *65*, 105789. [CrossRef]

20. Fahim, T.; Laouedj, S.; Abderrahmane, A.; Alotaibi, S.; Younis, O.; Ali, H.M. Heat transfer enhancement in parabolic through solar receiver: A three-dimensional numerical investigation. *Nanomaterials* **2022**, *12*, 419. [CrossRef]
21. Khashi'ie, N.S.; Waini, I.; Ishak, A.; Pop, I. Blasius Flow over a Permeable Moving Flat Plate Containing Cu-Al$_2$O$_3$ Hybrid Nanoparticles with Viscous Dissipation and Radiative Heat Transfer. *Mathematics* **2022**, *10*, 1281. [CrossRef]
22. Han, Y.; Yang, Y.; Mallick, T.; Wen, C. Nanoparticles to enhance melting performance of phase change materials for thermal energy storage. *Nanomaterials* **2022**, *12*, 1864. [CrossRef]
23. Kazem, H.A.; Chaichan, M.T.; Al-Waeli, A.H.; Jarimi, H.; Ibrahim, A.; Sopian, K. Effect of Temperature on the Electrical and Thermal Behaviour of a Photovoltaic/Thermal System Cooled Using SiC Nanofluid: An Experimental and Comparison Study. *Sustainability* **2022**, *14*, 11897. [CrossRef]
24. Herrando, M.; Ramos, A. Photovoltaic-Thermal (PV-T) Systems for Combined Cooling, Heating and Power in Buildings: A Review. *Energies* **2022**, *15*, 3021. [CrossRef]
25. Fernández, A.G.; González-Fernández, L.; Grosu, Y.; Labidi, J. Physicochemical Characterization of Phase Change Materials for Industrial Waste Heat Recovery Applications. *Energies* **2022**, *15*, 3640. [CrossRef]
26. Ghabuzyan, L.; Pan, K.; Fatahi, A.; Kuo, J.; Baldus-Jeursen, C. Thermal effects on photovoltaic array performance: Experimentation, modeling, and simulation. *Appl. Sci.* **2021**, *11*, 1460. [CrossRef]
27. Saghir, M.Z. Enhanced Energy Storage Using Pin-Fins in a Thermohydraulic System in the Presence of Phase Change Material. *Fluids* **2022**, *7*, 348. [CrossRef]
28. Balachandran, S.; Swaminathan, J. Advances in Indoor Cooking Using Solar Energy with Phase Change Material Storage Systems. *Energies* **2022**, *15*, 8775. [CrossRef]
29. Badr, F.; Radwan, A.; Ahmed, M.; Hamed, A.M. An experimental study of the concentrator photovoltaic/thermoelectric generator performance using different passive cooling methods. *Renew. Energy* **2022**, *185*, 1078–1094. [CrossRef]
30. Ge, M.; Zhao, Y.; Li, Y.; He, W.; Xie, L.; Zhao, Y. Structural optimization of thermoelectric modules in a concentration photovoltaic–thermoelectric hybrid system. *Energy* **2022**, *244*, 123202. [CrossRef]
31. Han, X.; Lv, Y. Design and dynamic performance of a concentrated photovoltaic system with vapor chambers cooling. *Appl. Therm. Eng.* **2022**, *201*, 117824. [CrossRef]
32. Fikri, M.A.; Samykano, M.; Pandey, A.; Kadirgama, K.; Kumar, R.R.; Selvaraj, J.; Abd Rahim, N.; Tyagi, V.; Sharma, K.; Saidur, R. Recent progresses and challenges in cooling techniques of concentrated photovoltaic thermal system: A review with special treatment on phase change materials (PCMs) based cooling. *Sol. Energy Mater. Sol. Cells* **2022**, *241*, 111739. [CrossRef]
33. Iqbal, W.; Ullah, I.; Shin, S. Nonimaging High Concentrating Photovoltaic System Using Trough. *Energies* **2023**, *16*, 1336. [CrossRef]
34. Li, Y.; Zhang, L.; Gao, W.; Liu, Y.; An, J.; Liu, Z.; Ju, X.; Li, M. Radiative sky cooling in low-medium concentration photovoltaic systems. *Appl. Therm. Eng.* **2023**, *221*, 119860. [CrossRef]
35. Li, G.; Hua, Q.; Sun, L.; Khosravi, A.; Pabon, J.J.G. Thermodynamic modeling and optimization of hybrid linear concentrating photovoltaic and mechanically pumped two-phase loop system. *Appl. Energy* **2023**, *333*, 120547. [CrossRef]
36. Santana, J.P.; Rivera-Solorio, C.I.; Chew, J.W.; Tan, Y.Z.; Gijón-Rivera, M.; Acosta-Pazmiño, I. Performance Assessment of Coupled Concentrated Photovoltaic-Thermal and Vacuum Membrane Distillation (CPVT-VMD) System for Water Desalination. *Energies* **2023**, *16*, 1541. [CrossRef]
37. Feng, T.; Chen, X.; Zhang, J.; Guo, J. Passive Satellite Solar Panel Thermal Control with Long-Wave Cut-Off Filter-Coated Solar Cells. *Aerospace* **2023**, *10*, 108. [CrossRef]
38. Khouya, A. Levelized costs of energy and hydrogen of wind farms and concentrated photovoltaic thermal systems. A case study in Morocco. *Int. J. Hydrog. Energy* **2020**, *45*, 31632–31650. [CrossRef]
39. Vodapally, S.N.; Ali, M.H. A Comprehensive Review of Solar Photovoltaic (PV) Technologies, Architecture, and Its Applications to Improved Efficiency. *Energies* **2023**, *16*, 319. [CrossRef]
40. Asim, M.; Milano, J.; Khan, H.I.; Hanzla Tahir, M.; Mujtaba, M.A.; Shamsuddin, A.H.; Abdullah, M.; Kalam, M.A. Investigation of Mono-Crystalline Photovoltaic Active Cooling Thermal System for Hot Climate of Pakistan. *Sustainability* **2022**, *14*, 10228. [CrossRef]
41. Ali, A.Y.M.; Abo-Zahhad, E.M.; Elkady, M.F.; Ookawara, S.; El-Shazly, A.H.; Radwan, A. Temperature uniformity enhancement of densely packed high concentrator photovoltaic module using four quadrants microchannel heat sink. *Sol. Energy* **2020**, *202*, 446–464. [CrossRef]
42. Zeneli, M.; Bellucci, A.; Sabbatella, G.; Fotopoulou, M.; Apostolopoulos, V.; Stamatopoulos, P.; Trucchi, D.M.; Nikolopoulos, A.; Rakopoulos, D. Thermal Assessment of Dielectric Microspacer Technology Using an Advanced Three-Dimensional Simulation Model. *Sustainability* **2023**, *15*, 1786. [CrossRef]
43. Radwan, A.; Ahmed, M. Thermal management of concentrator photovoltaic systems using microchannel heat sink with nanofluids. *Sol. Energy* **2018**, *171*, 229–246. [CrossRef]
44. Ahmed, A.; Shanks, K.; Sundaram, S.; Mallick, T.K. Theoretical investigation of the temperature limits of an actively cooled high concentration photovoltaic system. *Energies* **2020**, *13*, 1902. [CrossRef]
45. Awad, M.; Radwan, A.; Abdelrehim, O.; Emam, M.; Shmroukh, A.N.; Ahmed, M.J.S.E. Performance evaluation of concentrator photovoltaic systems integrated with a new jet impingement-microchannel heat sink and heat spreader. *Sol. Energy* **2020**, *199*, 852–863. [CrossRef]

46. Ali, A.Y.; Abo-Zahhad, E.M.; Elqady, H.I.; Rabie, M.; Elkady, M.F.; Ookawara, S.; El-Shazly, A.H.; Radwan, A. Thermal analysis of high concentrator photovoltaic module using convergent-divergent microchannel heat sink design. *Appl. Therm. Eng.* **2021**, *183*, 116201. [CrossRef]

47. AZURSPACE. Multijunction Solar Cell Datasheet. 2021. Available online: https://www.azurspace.com/index.php/en/products/products-cpv/cpv-solar-cells (accessed on 1 April 2022).

48. Awan, A.B.; Mouli, K.V.C.; Zubair, M.J.E.C. Performance enhancement of solar tower power plant: A multi-objective optimization approach. *Energy Convers. Manag.* **2020**, *225*, 113378. [CrossRef]

49. Vasilev, M.P.; Abiev, R.S.; Kumar, R. Effect of microchannel heat sink configuration on the thermal performance and pumping power. *Int. J. Heat Mass Transf.* **2019**, *141*, 845–854. [CrossRef]

50. Aldossary, A.; Mahmoud, S.; Al-Dadah, R. Technical feasibility study of passive and active cooling for concentrator PV in harsh environment. *Appl. Therm. Eng.* **2016**, *100*, 490–500. [CrossRef]